Fracture of crystalline silicon nanopillars during electrochemical lithium insertion

Seok Woo Lee[a], Matthew T. McDowell[a], Lucas A. Berla[a], William D. Nix[a,1], and Yi Cui[a,b,1]

[a]Department of Materials Science and Engineering, Stanford University, Stanford, CA 94305; [b]Stanford Institute for Materials and Energy Sciences, Stanford Linear Accelerator Center National Accelerator Laboratory, 2575 Sand Hill Road, Menlo Park, CA 94025

Contributed by William D. Nix, January 19, 2012 (sent for review December 9, 2011)

From surface hardening of steels to doping of semiconductors, atom insertion in solids plays an important role in modifying chemical, physical, and electronic properties of materials for a variety of applications. High densities of atomic insertion in a solid can result in dramatic structural transformations and associated changes in mechanical behavior: This is particularly evident during electrochemical cycling of novel battery electrodes, such as alloying anodes, conversion oxides, and sulfur and oxygen cathodes. Silicon, which undergoes 400% volume expansion when alloying with lithium, is an extreme case and represents an excellent model system for study. Here, we show that fracture locations are highly anisotropic for lithiation of crystalline Si nanopillars and that fracture is strongly correlated with previously discovered anisotropic expansion. Contrary to earlier theoretical models based on diffusion-induced stresses where fracture is predicted to occur in the core of the pillars during lithiation, the observed cracks are present only in the amorphous lithiated shell. We also show that the critical fracture size is between about 240 and 360 nm and that it depends on the electrochemical reaction rate.

anisotropy | lithium ion battery | plasticity | silicon anode

In modern high-energy density battery systems, the primary mechanism for energy storage is the insertion of secondary species into solid electrodes, as opposed to the surface reactions that occur in many traditional electrochemical systems (1, 2). In these batteries, understanding how the inserted species interacts with and changes the original material is vital for good performance. For long-term battery cycling with good capacity retention, cyclical insertion and extraction of secondary species during battery charge and discharge must occur with minimal irreversible structural changes that degrade storage capacity in the solid electrode material. Most commercial Li-ion batteries employ positive and negative electrode materials that react through an intercalation mechanism in which Li atoms are inserted and extracted from layered host structures with only small associated strains and structural changes (1, 2). These well-understood intercalation reactions allow for capacity retention over many cycles, but the specific capacity of intercalation materials is limited due to the weight of the atomic framework. Negative electrode materials that react with Li through an alloying mechanism have a much higher specific capacity, but large volume changes during lithium insertion/extraction can cause capacity fade with cycling due to fracture of the electrode materials (3, 4). Therefore, the control of structural and volume changes during Li insertion/extraction in these alloying electrode materials is essential for good performance.

Silicon, a Li-alloy negative electrode material, has an especially high theoretical lithium storage capacity of 4,200 mA hg^{-1} (approximately 10 times that of conventional graphite negative electrodes) (5–7). Capacity fade due to the 400% volume expansion generally plagues Si electrodes made from micron-sized particles (8, 9), but recently, Si nanostructures such as nanowires, nanotubes, and nanoparticles have shown improved cycling and fracture resistance because of lower stresses present during volume changes (10–16). Although these nanostructures have shown good behavior, the intricacies of how structural changes occur and the circumstances causing fracture are not well understood. Various theoretical models have been developed to study mechanical fracture of amorphous Si during electrochemical Li insertion by considering Li diffusion-induced stresses (17–20). These models have revealed that high stresses are possible and have also suggested a critical size below which Si nanostructures will avoid fracture; in one study, experimental evidence of fracture in Si nanowires corroborated theoretical predictions (18). However, recent experimental work has shown anisotropic volume expansion behavior along ⟨110⟩ crystalline directions during lithiation of crystalline Si nanostructures such as nanopillars, nanowires, and fabricated microstructures (21–23). These experimental observations possibly indicate the presence of more complicated mechanical stress states and different fracture behavior than has previously been modeled. Also, because the initial lithiation of crystalline Si nanostructures generally proceeds via a two-phase reaction in which a lithiated amorphous phase grows inward and consumes the crystal, the fracture characteristics of crystalline Si could be different than amorphous Si (24–28). As such, it is necessary to experimentally develop a full understanding of the nature of alloying-induced fracture in Si nanostructures. In this paper, we show that fracture can occur at the surface during lithiation of crystalline Si nanopillars, and that the presence and location of fracture is strongly affected by nanopillar crystalline orientation, diameter, and the electrochemical reaction rate.

The Si nanopillars used in this study were fabricated by dry etching of single-crystalline Si wafers of various crystal orientations (⟨100⟩, ⟨110⟩, and ⟨111⟩) using drop-cast silica spheres as the etch mask as shown in Fig. S1 (29, 30). The pillar diameter is primarily controlled by the diameter of the silica spheres. After initial fabrication, thermal oxidation and HF etching can be used to further remove material from the pillars to precisely tune their size. For electrochemical lithiation/delithiation, pieces of a Si wafer with area of approximately 25 mm^2 on which nanopillars had been fabricated were used as the working electrode in half cells with Li foil as the counter/reference electrode as shown in Fig. S2. For lithiation, the potential of the working electrode was swept to 10 mV vs. Li/Li^+ and held for 10 h. The sweep rate varied from 0.1 mV/s to infinite (immediately applying the lithiation potential of 10 mV without sweeping). For delithiation, the pillars were first lithiated with a very slow sweep rate (0.005 mV/s) to prevent fracture, and then they were held at 10 mV for 10 h. Next, the voltage was swept to 2 V using various sweep rates and held for 10 h. After electrochemical treatment, the samples were washed in acetonitrile in an Ar-filled glove box and observed with an SEM.

Author contributions: S.W.L., L.A.B., and Y.C. designed research; S.W.L. and M.T.M. performed research; S.W.L., M.T.M., L.A.B., W.D.N., and Y.C. analyzed data; and S.W.L., M.T.M., L.A.B., W.D.N., and Y.C. wrote the paper.

The authors declare no conflict of interest.

[1]To whom correspondence may be addressed. E-mail: yicui@stanford.edu or nix@stanford.edu.

This article contains supporting information online at www.pnas.org/lookup/suppl/doi:10.1073/pnas.1201088109/-/DCSupplemental.

Results

Fig. 1 shows SEM images of cracks in Si nanopillars of each axial orientation after full lithiation. Fig. 1 *A–C* shows top-down views of lithiated nanopillars that reveal how the pillars expand laterally and where fracture occurs. The insets in Fig. 1 *A–C* are results showing fully lithiated Si nanopillars of each axial crystal orientation without cracks (they were lithiated with a slow rate) (22); before lithiation, the pillars are circular in cross-section as shown in Fig. S3. Fig. 1 *D–F* shows corresponding side views of nanopillars of each axial orientation after lithiation. As we have previously reported, lateral expansion occurs preferentially at {110} surfaces, resulting in the ⟨100⟩ axially oriented pillars expanding into a cross shape, the ⟨110⟩ pillars expanding into an ellipse, and the ⟨111⟩ pillars expanding into a circle (22). As evidenced by the images in Fig. 1, cracks are also observed in some of the nanopillars after lithiation. In all three types of pillars, lithiation causes cracks to propagate along the axis at the surface of the pillars, as indicated by the red arrows in Fig. 1, suggesting that tensile hoop stress develops at the surface of the nanopillars during lithiation. This observation runs counter to modeling results based on diffusion-induced stresses which predict compressive hoop stresses at the surface of Si nanostructures during lithiation and the inhibition of crack formation and growth (17–19).

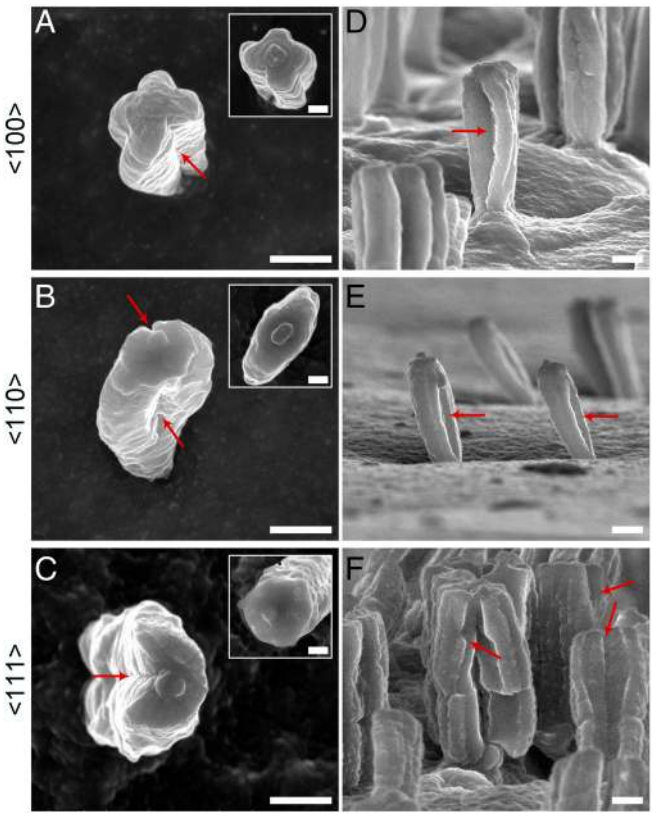

Fig. 1. Anisotropic lateral expansion and fracture of crystalline Si nanopillars with three different axial orientations (⟨100⟩, ⟨110⟩, and ⟨111⟩) after lithiation. (*A–C*) Top view SEM images of Si nanopillars of each crystal orientation after lithiation. Shown from top to bottom are the ⟨100⟩, ⟨110⟩, and ⟨111⟩ pillars. The red arrows indicate cracks, which are oriented along the axis of the nanopillars. The insets are top-view SEM images of lithiated Si pillars of the same size and crystal orientation showing anisotropic expansion without fracture at slow lithiation rates, as discussed in our previous study (22). (*D–F*) Side view SEM images of Si nanopillars of each crystal orientation. Shown from top to bottom are the ⟨100⟩, ⟨110⟩, and ⟨111⟩ pillars. In the images of ⟨100⟩ and ⟨110⟩ pillars, cracks are consistently found at the same sites (red arrows). For ⟨111⟩ pillars, the fracture location is more variable. The scale bars in the main images are 500 nm, and the scale bars in the insets are 200 nm.

The fracture locations of each of the pillars shown in Fig. 1 were consistently observed over many samples. Cracks in ⟨100⟩ pillars (Fig. 1 *A* and *D*) are located at some of the four inner corners of the expanded cross shape, which causes the two arms of the cross next to the crack to be widened and distorted. In ⟨110⟩ pillars, cracks are commonly found at the minor axis of the ellipse 90° from the {110} lateral surfaces, as shown in Fig. 1 *B* and *E*. Another study has similarly shown that a ⟨112⟩ axially oriented nanowire with two {110} lateral surfaces also develops cracks along the axis upon lithiation (23). Finally, as shown in Fig. 1 *C* and *F*, ⟨111⟩ pillars also develop cracks along the axial direction, but it is unclear from these images the precise relationship between crystalline orientation and fracture location.

To enrich these observations, statistical analysis was performed by measuring the angular orientation of cracks in many nanopillar samples of each axial orientation; these results are presented in Fig. 2. The angular orientation of each crack was measured from the horizontal dashed line (reference) to the solid line (fracture location), as shown in the cross-sectional schematics in Fig. 2. The data for each axial orientation are presented in the column charts in Fig. 2, and it is evident that there are clear tendencies for the nanopillars to fracture at certain angular orientations. As shown in Fig. 2*A*, most cracks on ⟨100⟩ pillars are found clustered around angles of 45, 135, 225, and 315°, which are 90° from each other. This finding corresponds to fracture on the surface of {100} lateral planes which are situated at 45° angles from the preferentially expanded {110} lateral planes (see schematic in Fig. 2*A*). Pillars with ⟨110⟩ axes show similar fracture tendencies (Fig. 2*B*): All cracks are found clustered around 145 and 325° (180° apart), corresponding to the two {100} lateral planes which are 90° from the {110} lateral planes. Finally, Fig. 2*C* shows that ⟨111⟩ axially oriented pillars exhibit cracks primarily around angles of 30, 90, 210, and 270°, which correspond to {112} lateral planes located between the {110} lateral planes. Less frequently, cracks were also found at {110} lateral surfaces. Overall, the different axially oriented pillars fracture in a similar manner during lithiation: Cracks develop primarily at the sidewalls of the pillars between neighboring {110} planes regardless of the angle over which the {110} planes are separated.

To further confirm that the cracks nucleate at the surface, we performed experiments in which ⟨111⟩ axially oriented pillars were partially lithiated, resulting in structures with crystalline Si cores and amorphous lithiated shells, as shown in Fig. 3*A*. The nanopillars were partially lithiated by sweeping to and holding at 80 mV vs. Li/Li^+ for 10 h, which is slightly higher than the full lithiation potential of 10 mV. The pristine nanopillar diameter was 430 nm, and the voltage sweep rate was 0.1 mV/s. The image in Fig. 3*A* shows that the core and shell of the partially lithiated pillars produce different SEM contrast, and there are cracks in the lithiated amorphous shell. After etching the amorphous Li-Si alloy in methanol (31) (see Fig. S4 for details), the crystalline cores of the pillars are revealed, as shown in Fig. 3*B*. The remaining crystalline cores are circular in shape and do not contain cracks or defects, indicating that the cracks that form in the lithiated shell do not propagate into the crystalline core. A recent study also showed similar fracture at the amorphous surface during lithiation of crystalline Si nanoparticles, which was attributed to tensile hoop stress that develops at the surface due to the growth of the amorphous phase at the crystalline/amorphous interface (32). For a partially lithiated cylindrical nanopillar with a Si core radius of a and an outside radius of b, the tensile hoop stress in the amorphous phase would be approximately $\sigma_\theta = Y[1 - \ln(b/r)]$ if the amorphous phase is fully plastic at the yield stress Y. This simple model is based on the expansion of a pressurized thick-walled tube with yield strength Y (33, 34) (see Fig. S5 for details).

Taken together, the images and statistical analysis in Figs. 1–3 indicate that (*i*) fracture occurs at the surface of the nanopillars

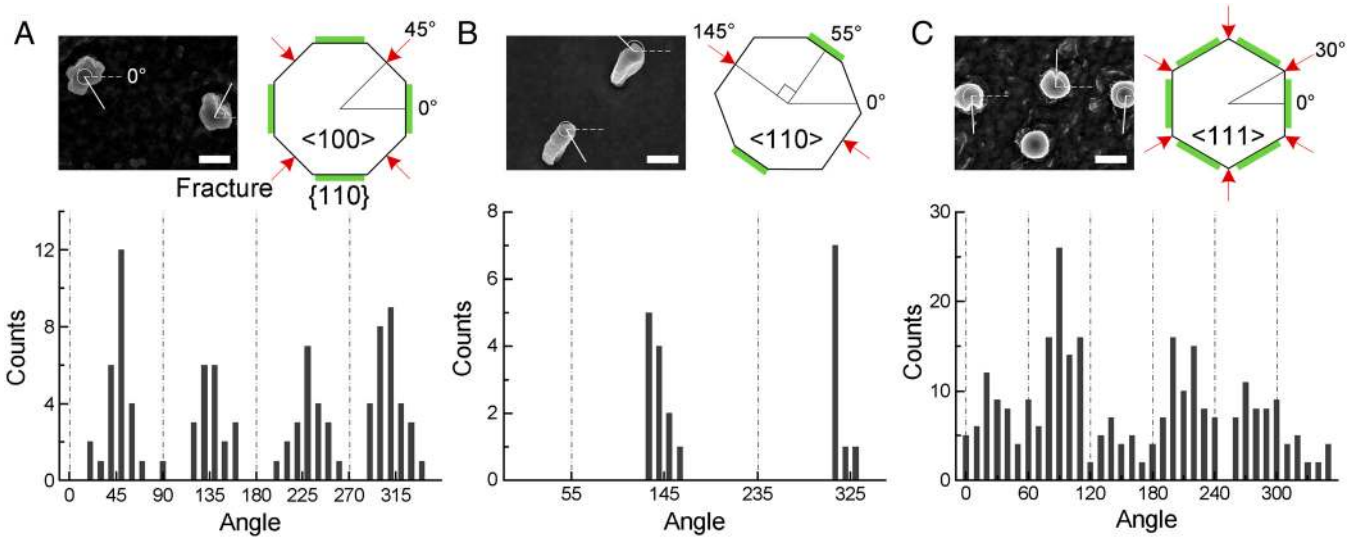

Fig. 2. Statistical study of the fracture location at the surface of Si nanopillars with different axial orientations during lithiation. Each panel *A–C* shows an example SEM image, a schematic of the pillar cross-section, and a compilation of fracture location data presented as a column chart. The data are compiled by examining many top-down SEM images and measuring the angle from an arbitrary reference point to the fracture location, as shown in the SEM images and schematics. The dashed lines in the inset SEM images indicate the reference point (0°), and the solid lines show the location of the cracks; the angular location of the cracks is measured between these lines. The green highlights in the schematic views and the dashed lines in the column charts indicate the angular location of the {110} surfaces on the sidewalls of the pillars. Red arrows point to fracture sites. (*A*) Pillars with ⟨100⟩ axes expand preferentially at the four lateral {110} surfaces (0, 90, 180, and 270° in the figure), and the four most common fracture sites are located at the lateral {100} surfaces (45, 135, 225, and 315° in the column chart). (*B*) Pillars with ⟨110⟩ axes expand preferentially at the two lateral {110} surface (55 and 225° in the figure), and the two most common fracture sites are at the lateral {100} surfaces (145 and 325° in the column chart). (*C*) Pillars with ⟨111⟩ axes have six {110} lateral surfaces that expand preferentially (0, 60, 120, 180, 240, and 300° in the figure), and the most common fracture sites are the {112} lateral surfaces that are positioned between neighboring {110} surfaces (30, 90, 150, 210, 270, and 330° in the column chart). Overall, these data show that nanopillars of all orientations consistently fracture at surface locations that lie midway between lateral {110} planes, as shown by the red arrows in the schematics. Scale bars in the SEM images are 1 μm.

during lithiation and (*ii*) cracks are located on the sidewalls between neighboring {110} lateral surfaces. Based on our observation that cracks occur at specific angular locations in each of the nanopillars, we propose that anisotropic expansion of the nanopillars might result in intensified tensile hoop stress on the surface at locations between {110} lateral surfaces. This concept is illustrated in the schematic in Fig. 3*C*, which shows a top-down view of a lithiated ⟨110⟩ axially oriented nanopillar. The initially circular ⟨110⟩ pillar expands to an elliptical shape, and the crystal core shrinks anisotropically so that it is thinner along the ⟨110⟩ lateral directions because these directions are lithiated preferentially. In this pillar, the ⟨110⟩ preferential volume expansion could lead to tensile hoop stress concentrations at the two {100} lateral surfaces that are perpendicular to the {110} lateral surfaces. In the ⟨100⟩ and ⟨111⟩ pillars, fracture also occurs primarily between {110} lateral planes, which indicates that there also could be intensified tensile hoop stress at these locations in these other nanopillars (see Fig. S6 for schematics).

In the previous discussion, we have considered nanopillars of a single size after only lithiation. To develop a more thorough understanding of the fracture process, we also examined nanopillars of various sizes after lithiation and delithiation. Fig. 4 shows images of ⟨111⟩ axially oriented nanopillars with initial diameters of 240 and 390 nm before electrochemical reaction, after lithiation, and after delithiation. For nanopillars that were observed after lithiation, the potentials of nanopillar electrodes in half cells were swept at 1 mV/s to 10 mV and held for 10 h. For observation after delithiation, pillars were first lithiated with a very slow sweep rate (0.005 mV/s) to avoid fracture, held at 10 mV for 10 h, and then they were delithiated by sweeping the voltage at 1 mV/s to 2 V and holding for 10 h. Pristine 240-nm-diameter pillars (Fig. 4*A*) expand to almost twice their initial diameter after lithiation (Fig. 4*B*) and then contract back to their original size after delithiation (Fig. 4*C*). Most pillars of this size maintained

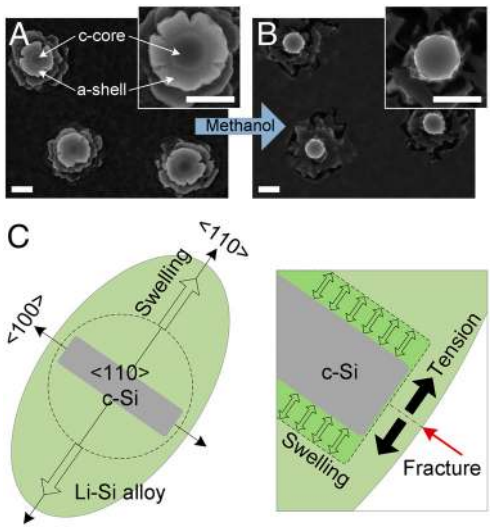

Fig. 3. Fracture in the amorphous shell of partially lithiated nanopillars. (*A*) Top-view SEM image of ⟨111⟩ Si nanopillars with 430 nm initial diameter after partial lithiation. The pillars consist of a lithiated amorphous shell and a crystalline Si core. The amorphous shell contains cracks, distinguishable from the crystalline core by slightly different contrast. (*B*) Top-view SEM image of a similar sample after etching away the amorphous lithiated shells in methanol; only the crystalline cores of the ⟨111⟩ Si nanopillars remain. (Scale bars: 500 nm.) (*C*) Schematic view showing our suggested fracture mechanism. The movement of the two-phase crystalline/amorphous interface into the crystal core has been proposed to generate tensile hoop stress at the surface of nanostructures (32), and anisotropic volume expansion at lateral {110} surfaces could serve to intensify this stress at locations between these surfaces. The schematic shows a lithiated ⟨110⟩ axially oriented nanopillar that experiences tensile hoop stress and eventual fracture at the {100} lateral surfaces due to the anisotropic expansion.

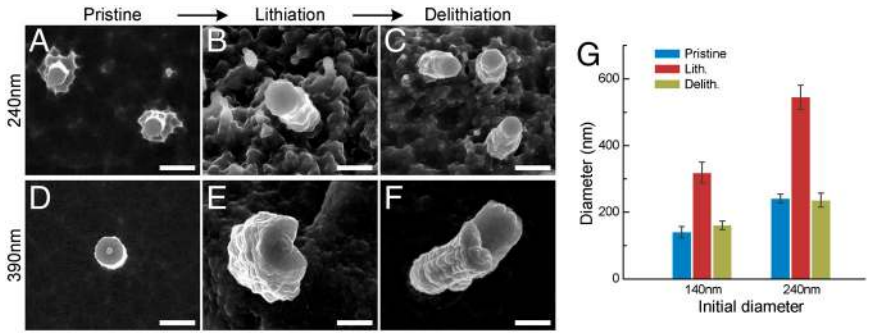

Fig. 4. SEM images showing the effect of nanopillar size on fracture characteristics. (*A*) SEM image of pristine 240-nm diameter ⟨111⟩ Si pillars. (*B*) A 240-nm diameter ⟨111⟩ nanopillar after lithiation at 10 mV. The pillar expands to a circular shape. (*C*) Two hundred forty nanometer diameter ⟨111⟩ nanopillars after delithiation. The pillars contract back to close to their initial size. (*D*) SEM image of a pristine 390-nm diameter Si pillar. (*E*) A 390-nm pillar after lithiation at 10 mV. The pillar expands and fractures. (*F*) A 390-nm pillar after delithiation showing that the crack becomes more severe. (*G*) Column chart showing the average diameter of nanopillars after lithiation and delithiation. The pillars had initial diameters of 140 and 240 nm, and the error bars indicate the standard deviation. (Scale bars: 500 nm.)

their original cylindrical shape after one lithiation/delithiation cycle, and cracks were found in only a few pillars. Smaller 140-nm-diameter pillars also showed the same behavior (Fig. S7). In contrast, most larger 390-nm-diameter pillars (Fig. 4*D*) fracture after lithiation (Fig. 4*E*), and severe cracks propagate through the central axis and separate the entire pillar structure after delithiation (Fig. 4*F*, see Fig. S8 for details). The column chart in Fig. 4*G* shows the average pristine, lithiated, and delithiated diameters from more than 30 pillars with 140 and 240 nm initial diameters. The 140- and 240-nm-diameter nanopillars expand to 319 and 545 nm after lithiation and contract back to 161 and 236 nm after delithiation, respectively. The error bars on the chart indicate standard deviation. The change in diameter for larger pillars could not be measured accurately because of severe cracks.

To further investigate the effects of size and reaction rate on the fracture of Si nanostructures during lithiation and delithiation, ⟨111⟩ Si pillars with diameters between 140 and 390 nm were lithiated and delithiated using various voltage sweep rates ranging from 0.1 mV/s to infinite (applying the lithiation voltage immediately without sweeping). The faster sweep rates result in faster electrochemical reaction of the nanopillars. Similarly to the previous experiments, the voltage was swept to 10 mV for lithiation and 2 V for delithiation and held at each vertex potential for 10 h. After lithiation or delithiation, the fraction of cracked pillars was counted using SEM. For the obvious cases in which the fracture ratio was less than 2% or more than 90%, about 50 pillars were counted. For intermediate cases, more than 150 pillars were counted. Fig. 5*A* shows the fraction of fractured pillars of different initial diameters after lithiation at various voltage sweep rates. For pillars with 140-nm initial diameter, only a few cracks were found, and the overall fracture ratio was less than 2% when the sweep rates were between 0.1 and 10 mV/s and 4% when the voltage was immediately applied without sweeping. In contrast, the fracture ratio of larger 240-nm-diameter pillars is more strongly dependent on the voltage sweep rate. At the slowest sweep rate (0.1 mV/s), there were no observed cracks in the pillars, but the fracture ratio grows for faster sweep rates. The fracture ratios are 13.4, 13.9, and 22.4% for voltage sweep rates of 1 and 10 mV/s, and immediate hold without a sweep, respectively. The larger pillars with 360- and 390-nm diameters show severe fracture (greater than 88% fracture ratio) at all voltage sweep rates.

Fig. 5*B* shows the fracture ratio of pillars with smaller initial diameters (140 and 240 nm) after delithiation using various voltage sweep rates. The fracture ratio for larger pillars could not be measured accurately after delithiation because the lithiation step already causes fracture in most pillars even at very low sweep rates. Both the 140- and 240-nm-diameter pillars exhibit low fracture ratios (<5.5%) for all voltage sweep rates after delithiation; this is in contrast to the results after lithiation, where 240-nm-diameter pillars show an increased fracture ratio with higher voltage sweep rate. Overall, this data series shows that there is a critical size for fracture upon lithiation of crystalline Si particles that depends on lithiation rate, and that this critical size is between about 240 and 360 nm. During delithiation, the amorphous Li-Si alloy is converted to amorphous Si, and the data suggest that the critical size for fracture is somewhat larger than 240 nm because very few 240-nm nanopillars were observed to fracture upon delithiation. As discussed previously, the initial conversion of the crystalline Si to amorphous lithiated Si proceeds via movement of a two-phase interface, whereas the delithiation of amorphous Si is a one-phase reaction (4, 27, 28). As such, the stresses that develop during these processes are different, and the data here indicate that the critical size for fracture is different. This interesting observation suggests that the lithiation/delithiation of amorphous Si

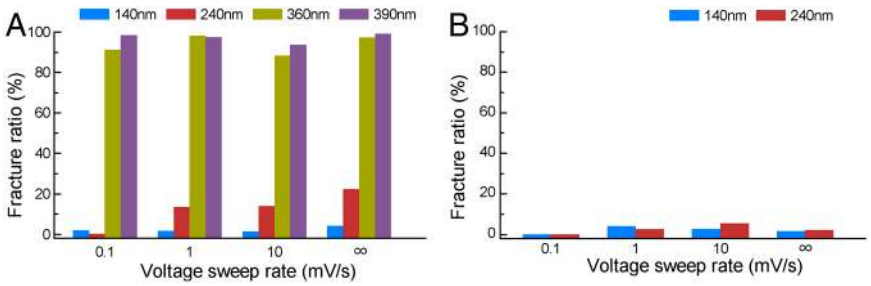

Fig. 5. The effect of nanopillar size and reaction rate on the fracture ratio for ⟨111⟩ axially oriented nanopillars. The "fracture ratio" was determined by examining a large number of nanopillars and dividing the number of fractured nanopillars by the total number of pillars counted. (*A*) Column chart showing the fracture ratio for ⟨111⟩ nanopillars of different initial diameters after lithiation with different voltage sweep rates. Nanopillars with 360 and 390 nm initial diameter have a high fracture ratio for all lithiation rates (>88%), whereas 140-nm diameter pillars have low fracture ratios (less than approximately 5%). Nanopillars of intermediate initial size (240 nm) show increasing fracture ratio with faster lithiation rates. (*B*) Column chart showing the fracture ratio for ⟨111⟩ nanopillars after delithiation. Nanopillars with initial diameter of 140 and 240 nm show infrequent fracture after delithiation.

could result in lower stresses or a different stress state than in crystalline Si, and that fracture might occur less readily in initially amorphous structures.

A critical diameter of $d_0^c \approx 300$ nm is not inconsistent with a fracture mechanics description of these events. According to the plasticity result cited above, as the crystalline Si core is lithiated, the growing amorphous shell can be under a hoop tensile stress over a domain extending from $r = b/e$ to $r = b$, where b is the outside radius of the fully lithiated nanopillar. We assume that for the fully lithiated state the diameter increases by a factor of about two, so that $b \approx d_0$, where d_0 is the initial diameter of the crystalline Si nanopillar. Taking the average tensile hoop stress, $\tilde{\sigma}_\theta = Y/(e-1)$, and the crack length to be as much as $b - b/e$, we find a stress intensity factor of $K \approx \tilde{\sigma}_\theta \sqrt{\pi(b - b/e)} \approx Y/(e-1)\sqrt{\pi d_0^c (1 - 1/e)}$. With $Y \approx 1$ GPa (35) and $d_0^c \approx 300$ nm, this leads to an estimated fracture toughness of $K \approx 0.45$ MPa$\sqrt{m}$, not an unreasonable lower bound for lithiated amorphous Si.

Conclusion

In summary, we investigate fracture in Si nanopillars of different axial orientation and size during the first cycle of lithiation and delithiation. It was found that, upon lithiation, fracture sites are located at the surface of nanopillars between neighboring $\{110\}$ lateral planes. Modeling of diffusion-induced stress during single-phase lithiation of Si structures has predicted compressive hoop stress to exist at the surface during lithiation (18), which makes our experimental observations of surface cracks intriguing. Previous work has attributed surface cracking in crystalline nanostructures to tensile hoop stress that develops due the movement of the two-phase interface. We propose that anisotropic expansion of the crystal could result in intensified tensile hoop stress at the fracture locations observed in our study. Statistical analysis of the fracture ratio for $\langle 111 \rangle$ Si pillars reveals that pillars of smaller size lithiated at slower rates usually avoid fracture, whereas larger nanopillars usually fracture at all lithiation rates. The critical diameter for fracture is between 240 and 360 nm during lithiation and is probably higher for delithiation. Overall, the observations in this paper are expected to provide better insight for the design of Si anodes because the unexpected fracture upon first lithiation of these nanopillars could result in significant capacity loss on the first cycle.

Materials and Methods

Silica Nanoparticle Synthesis. Silica nanoparticles were produced by a modified Stöber synthesis (36). Briefly, a 1.3 mL tetraethyl orthosilicate was mixed with 10 ml ethanol, and then a NH_4OH/ethanol solution was added to precipitate silica. After 8 h of reaction, the spheres were centrifuged and cleaned with ethanol and methanol. Silica nanospheres with 600-nm diameter were produced.

Silicon Nanopillar Fabrication. Silicon wafers (*p* type, 10–20 Ω · cm, 500 to approximately 550-μm thick) with $\langle 100 \rangle$, $\langle 110 \rangle$, and $\langle 111 \rangle$ axes were first cleaned with O_2 plasma for 5 min and then the colloid of silica nanospheres was dispersed on the wafer and allowed to dry. These Si wafers were then etched using the Bosch process with a Deep Reactive Ion Etcher (Surface Technology Systems Co.) SF_6 (50 sccm) and C_4H_8 (80 sccm) were used for etching and passivation with 3 and 6 s active times, respectively. The total etching time was 7 to approximately 9 min at 350 W of rf power. After dry etching, wet etching with concentrated HF for several seconds dissolved the remaining silica nanospheres on top of the pillars.

Electrochemistry and Structural Characterization. Half cells were made with pieces of the wafers on which Si nanopillars had been etched as the working electrode. Li foil was used as the counter/reference electrode. Polymer separators from Nagase were placed between the two electrodes, and the sandwich structure was sealed in a pouch with external electrical leads. The electrolyte was 1 M $LiPF_6$ in ethylene carbonate/diethyl carbonate (1:1; Merck). For lithiation/delithiation, linear sweep voltammetry was used on either a Bio-logic VMP3 battery tester or an Arbin BT2000. For lithiation, the voltage was swept at varying rates from the open circuit voltage to 10 mV vs. Li/Li^+, where it was held for 10 h to ensure complete lithiation of the nanopillars. For delithiation, the voltage was swept from 10 mV to 2 V, where it was again held for 10 h.

After electrochemical treatment, the nanopillar sample was removed in an Ar-filled glove box and washed with acetonitrile to eliminate residual electrolyte and solid electrolyte interface. The samples were then transferred to the SEM (XL30 Sirion SEM; FEI) for imaging. To minimize exposure to the air, the sample was sealed in a glass vial while still in the glove box and was then carried to the SEM and transferred within 15 s.

ACKNOWLEDGMENTS. A portion of this work is supported by the US Department of Energy (DOE), Office of Basic Energy Sciences, Division of Materials Sciences and Engineering under Contract DE-AC02-76SF00515 through the Stanford Linear Accelerator Center National Accelerator Laboratory, Laboratory Directed Research and Development project and Assistant Secretary for Energy Efficiency and Renewable Energy, Office of Vehicle Technologies of the US DOE under Contract DE-AC02-05CH11231, Subcontract 6951379 under the Batteries for Advanced Transportation Technologies Program. Y.C. acknowledges support from the King Abdullah University of Science and Technology (KAUST) Investigator Award (KUS-I1-001-12). S.W.L. acknowledges support from KAUST (KUK-F1-038-02). M.T.M. acknowledges support from the Chevron Stanford Graduate Fellowship, the National Defense Science and Engineering Graduate Fellowship, and the National Science Foundation Graduate Fellowship. L.A.B. acknowledges support from the National Science Foundation Graduate Research Fellowship and, together with W.D.N., gratefully acknowledges support from the Office of Science, Office of Basic Energy Sciences, of the US DOE under Contract DE-FG02-04-ER46163.

1. Huggins RA (2010) *Advanced Batteries: Materials Science Aspects* (Springer, New York), pp 1–5.
2. Tarascon JM, Armand M (2001) Issues and challenges facing rechargeable lithium batteries. *Nature* 414:359–367.
3. Choi N-S, Yao Y, Cui Y, Cho J (2011) One dimensional Si/Sn-based nanowires and nanotubes for lithium-ion energy storage materials. *J Mater Chem* 21:9825–9840.
4. Limthongkul P, Jang Y-I, Dudney NJ, Chiang Y-M (2003) Electrochemically-driven solid-state amorphization in lithium-silicon alloys and implications for lithium storage. *Acta Mater* 51:1103–1113.
5. Armand M, Tarascon JM (2008) Building better batteries. *Nature* 451:652–657.
6. Boukamp BA, Lesh GC, Huggins RA (1981) All-solid lithium electrodes with mixed-conductor matrix. *J Electrochem Soc* 128:725–729.
7. Whittingham MS (2008) Materials challenges facing electrical energy storage. *MRS Bull* 33:411–419.
8. Beaulieu LY, Eberman KW, Turner RL, Krause LJ, Dahn JR (2001) Colossal reversible volume changes in lithium alloys. *Electrochem Solid-State Lett* 4:A137–A140.
9. Kasavajjula U, Wang C, Appleby AJ (2007) Nano-and bulk-silicon-based insertion anodes for lithium-ion secondary cells. *J Power Sources* 163:1003–1039.
10. Chan CK, et al. (2008) High-performance lithium battery anodes using silicon nanowires. *Nat Nanotechnol* 3:31–35.
11. Cui LF, Ruffo R, Chan CK, Peng H, Cui Y (2009) Crystalline-amorphous core-shell silicon nanowires for high capacity and high current battery electrodes. *Nano Lett* 9:491–495.
12. Kim H, Chou C-Y, Ekerdt JG, Hwang GS (2011) Structure and properties of li-si alloys: A first-principles study. *J Phys Chem C Nanomater Interfaces* 115:2514–2521.
13. Kovalenko I, et al. (2011) A major constituent of brown algae for use in high-capacity Li-ion batteries. *Science* 334:75–79.
14. Magasinski A, et al. (2010) High-performance lithium-ion anodes using a hierarchical bottom-up approach. *Nat Mater* 9:353–358.
15. Song T, et al. (2010) Arrays of sealed silicon nanotubes as anodes for lithium ion batteries. *Nano Lett* 10:1710–1716.
16. Yao Y, et al. (2011) Interconnected silicon hollow nanospheres for lithium-ion battery anodes with long cycle life. *Nano Lett* 11:2949–2954.
17. Bhandakkar TK, Gao H (2011) Cohesive modeling of crack nucleation in a cylindrical electrode under axisymmetric diffusion induced stresses. *Int J Solids Struct* 48:2304–2309.
18. Ryu I, Choi JW, Cui Y, Nix WD (2011) Size-dependent fracture of Si nanowire battery anodes. *J Mech Phys Solids* 59:1717–1730.
19. Zhao K, Pharr M, Vlassak JJ, Suo Z (2010) Fracture of electrodes in lithium-ion batteries caused by fast charging. *J Appl Phys* 108:073517.
20. Cheng Y-T, Verbrugge MW (2010) Diffusion-induced stress, interfacial charge transfer, and criteria for avoiding crack initiation of electrode particles. *J Electrochem Soc* 157: A508–A516.
21. Goldman JL, Long BR, Gewirth AA, Nuzzo RG (2011) Strain anisotropies and self-limiting capacities in single-crystalline 3d silicon microstructures: Models for high energy density lithium-ion battery anodes. *Adv Funct Mater* 21:2412–2422.
22. Lee SW, McDowell MT, Choi JW, Cui Y (2011) Anomalous shape changes of silicon nanopillars by electrochemical lithiation. *Nano Lett* 11:3034–3039.
23. Liu XH, et al. (2011) Anisotropic swelling and fracture of silicon nanowires during lithiation. *Nano Lett* 11:3312–3318.
24. Chan CK, Ruffo R, Hong SS, Huggins RA, Cui Y (2009) Structural and electrochemical study of the reaction of lithium with silicon nanowires. *J Power Sources* 189:34–39.
25. Key B, et al. (2009) Real-time NMR investigations of structural changes in silicon electrodes for lithium-ion batteries. *J Am Chem Soc* 131:9239–9249.

26. Li H, et al. (2000) The crystal structural evolution of nano-Si anode caused by lithium insertion and extraction at room temperature. *Solid State Ionics* 135:181–191.
27. Li J, Dahn JR (2007) An in situ X-Ray diffraction study of the reaction of Li with crystalline Si. *J Electrochem Soc* 154:A156–A161.
28. McDowell MT, et al. (2011) Novel size and surface oxide effects in silicon nanowires as lithium battery anodes. *Nano Lett* 11:4018–4025.
29. Chang C, et al. (2005) Etching submicrometer trenches by using the Bosch process and its application to the fabrication of antireflection structures. *J Micromech Microeng* 15:580–585.
30. Hsu CM, Connor ST, Tang MX, Cui Y (2008) Wafer-scale silicon nanopillars and nanocones by Langmuir-Blodgett assembly and etching. *Appl Phys Lett* 93:133109.
31. Castellano RN, Schmidt PH (1971) Chemical polish and etch for lithium, sodium and potassium. *J Electrochem Soc* 118:653–654.
32. Liu XH, Huang JY (2011) In situ TEM electrochemistry of anode materials in lithium ion batteries. *Energy Environ Sci* 4:3844–3860.
33. Hill R (1998) *The Mathematical Theory of Plasticity* (Oxford Univ Press, New York), pp 106–113.
34. Zhao K, et al. (2012) Concurrent reaction and plasticity during initial lithiation of crystalline silicon in lithium-ion batteries. *J Electrochem Soc* 159:A238–A243.
35. Sethuraman VA, Chon MJ, Shimshak M, Srinivasan V, Guduru PR (2010) In situ measurements of stress evolution in silicon thin films during electrochemical lithiation and delithiation. *J Power Sources* 195:5062–5066.
36. Bogush GH, Tracy MA, Zukoski CF (1988) Preparation of monodisperse silica particles—control of size and mass fraction. *J Non Cryst Solids* 104(1):95–106.